Weather and Climate Extremes 42 (2023) 100633

Contents lists available at ScienceDirect

Weather and Climate Extremes

journal homepage: www.elsevier.com/locate/wace

Why are severe weather and anomalous climate events often associated with the orthogonal convergence of airflows?

Weihong Qian [a,c,*], Jun Du [b], Jeremy Cheuk-Hin Leung [a], Weijing Li [a], Fangfang Wu [d], Banglin Zhang [a]

[a] Guangzhou Institute of Tropical and Marine Meteorology/Guangdong Provincial Key Laboratory of Regional Numerical Weather Prediction, CMA, Guangzhou, China
[b] Environmental Modeling Center, National Centers for Environmental Predictions, NWS/NOAA, College Park, MD, USA
[c] Department of Atmospheric and Oceanic Sciences, Peking University, Beijing, China
[d] Yancheng Meteorological Office of Jiangsu, Yancheng, China

ARTICLE INFO

Keywords:
Severe weather
Airflow
Orthogonal convergence
Shear stress modulus

ABSTRACT

Severe weather often occurs in the areas where different cold-warm and dry-wet air masses converge orthogonally. The orthogonal convergence of two-adjacent air parcels can be observed from planetary-scale to synoptic-scale and meso-scale circulations. This study pointed out that an orthogonal convergence of two-adjacent horizontal air parcels can produce a significant non-zero shear stress with its modulus as anomalous energy density and form vertical motions of new airflows, while tailgating and head-on horizontal convergences cannot. Therefore, the orthogonal convergence can induce strong vertical motions and result in severe weather. Continuous convergence of airflows can lead to unusual climatic events. Storm cases of single tornado, tornado swarms, a strong tropical cyclone, and extratropical cyclones associated with heavy rainfall or heavy airborne dust show that the shear stress modulus and total kinetic energy of anomalous winds can better explain extreme weather events than other commonly used dynamical parameters such as divergence and vorticity. Therefore, the shear stress modulus can be used in the forecasting of extreme weather events in operation.

1. Introduction

Severe or extreme weather such as heavy rainfall, tornado, thunderstorm, snowstorm, and sandstorm can be understood as anomalous synoptic phenomena which usually happened in the place of strong vertical or rising motions (Dowdy and Catto, 2017). Extreme weather can cause natural disasters and casualties (Beall, 2012). However, anomalous synoptic phenomena often occur along a large-scale circulation system. Over ocean surface, several tropical storms with their precipitation can be formed within a planetary-scale convergence zone of two airflows (Molinari and Vollaro, 2000). In terrestrial surface, cyclone family with heavy rainfall occur on the leeward side of mountains and form in a continental-scale convergence zone of two airflows (Qin et al., 2006). In time scale, the relative stability of convergence zones in planetary- and continental-scale wind fields can lead to persistent occurrence of extreme weather (Cai et al., 2012). These spatially stable and temporally sustained clusters of extreme weather cause persistent climatic events, which are characterized by sub-seasonal and inter-annual climate variations (Moron et al., 2017; Li et al., 2021). Local extreme weather and spatiotemporal anomalous climate events are the focus of meteorological forecasting (Brunet et al., 2023; Lavers et al., 2020).

The occurrence of local extreme weather and regional anomalous climate events can be seen as the release of anomalous energy (*i.e.*, an energy much higher than its climatological value) in the atmosphere. In daily weather and climate forecasting, how can we quickly identify where the greatest anomalous energy is in a weather map or a numerical weather model product? On weather maps, anomalous kinetic energies occur where winds converge, such as shear lines or convergence lines of wind field. The convergence lines are associated with the interaction of different airflows from different directions. What are the differences in the distribution characteristics of anomalous energy formed from different convergences of airflows?

In conventional weather dynamics and daily weather forecasting, many dynamical and thermodynamical parameters, such as vorticity, divergence, helicity, and convective available potential energy, are

* Corresponding author. Guangzhou Institute of Tropical and Marine Meteorology/Guangdong Provincial Key Laboratory of Regional Numerical Weather Prediction, CMA, Guangzhou, China.
E-mail address: qianwh@pku.edu.cn (W. Qian).

https://doi.org/10.1016/j.wace.2023.100633
Received 23 August 2023; Received in revised form 17 November 2023; Accepted 17 November 2023
Available online 22 November 2023

derived to describe motions of airflows, particularly to indicate convective weather (Seo, 2021; Zhao et al., 2021; Sun et al., 2023). However, for many cases, full or total variables from observations and model products as well as their parameters cannot well indicate the intensity, location, and duration of local severe weather such as thunderstorms, sandstorms, and tornadoes. This paper introduces a new dynamical parameter, the shear stress modulus, which is based on the formula from the convergence of two-adjacent airflows and trying to apply it in daily forecasting of extreme weather. For the physical explanation, Section 2 describes the shear stress and its modulus formed by the interaction of airflows at multiple motion angles. Sections 3, 4, 5 and 6 present some examples of the interaction of planetary-, continental-, synoptic- and meso-scale airflows in the Earth's atmosphere, which include from single tornado and tornado swarms as well as from strong tropical cyclones and extratropical cyclones associated with heavy rainfall or dust storm. Finally, conclusions and discussion are given in Section 7.

2. Shear stress and modulus of airflow interaction

Tropical cyclones develop from initial small disturbances. Most typhoons and hurricanes originate from the interaction of southeasterly trade wind and northeasterly trade wind in the tropical Pacific and Atlantic Oceans. If two air parcels from the southeasterly trade wind and the northeasterly trade wind orthogonally colliding on the convergence zone can be seen as two particles, their interaction is likely similar to the device of an orthogonal collider (Qian, 2022). Current high-energy particle colliders in the world are the device of linear collisions (Normile and Cho, 2019; Gibney, 2022). The purpose of colliders is to produce higher energy densities and new physical states of matter from the high-speeding collision of two-beam particles. A linear collision of two particles (or two-beam particles) is a centroid collision (Moraes et al., 2005; Lindstrom et al., 2020). The total energy E_T of two particles (masses are m_A and m_B, velocities are v_A and v_B) collided linearly on-head with the two energies ($E_A = \frac{1}{2}m_A v_A^2$ and $E_B = \frac{1}{2}m_B v_B^2$) is their sum, i.e., $E_T = E_A + E_B$.

The process of the orthogonal collider is to separate two-beam energetic particles coming from a linear accelerator into an annular cavity and then cause them to collide orthogonally (Qian, 2022). The two particles have two centripetal forces of radius r relative to the center of the annular cavity,

$$\vec{F}_A = \frac{m_A}{r} v_A{}^2 \vec{n}_A, \tag{1}$$

and

$$\vec{F}_B = \frac{m_B}{r} v_B{}^2 \vec{n}_B. \tag{2}$$

Where, the two letters $\vec{n}_A$ and $\vec{n}_B$ denote unit vectors of moving particles. The shear stress generated by the orthogonal collision of two particles at a point H is,

$$\vec{\tau}_H = \left(\frac{m_A}{r} v_A^2\right) \cdot \left(\frac{m_B}{r} v_B^2\right) \cdot \left(\vec{n}_A \times \vec{n}_B\right). \tag{3}$$

The shear stress at this point H has two directions, perpendicular to the plane of the two vectors $\vec{n}_A \times \vec{n}_B$. The shear stress modulus is,

$$\tau_H = \left(\frac{m_A}{r} v_A^2\right) \cdot \left(\frac{m_B}{r} v_B^2\right) sin\ \theta. \tag{4}$$

Where, the letter θ is the angle between $\vec{n}_A$ and $\vec{n}_B$. Obviously, when $\theta = 90°$, the shear stress modulus reaches the maximum,

$$\tau_{Hmax} = \left(4 / r^2\right) E_A E_B. \tag{5}$$

If two colliding particles have the same mass and velocity, the resulting energy density per unit area r^2 in an orthogonal collision at the point H is $4E^2$, while the energy density of two particles colliding linearly is $2E$. Thus, the energy density of orthogonal collision is $2E$ times larger than that of linear collision.

In the atmosphere, the horizontal movement of airflows from different directions converges in different angles. Both precipitation and strong convective weather are related to the convergence of synoptic-scale and regional-scale or meso-scale airflows in the lower atmosphere. On the daily weather map, we can observe four types of airflow convergence (Fig. 1).

In Fig. 1a, the air parcel A moves faster than the air parcel B at the same direction so that they produce a "tailgating convergence" at the point H. In Fig. 1b, the air parcel A and the air parcel B move on a straight line but opposite directions so that they produce a "head-on convergence" at the point H. In Fig. 1c, the air parcel A and the air parcel B converge at the point H from two directions with their angle θ so that they form a "cross convergence". In Fig. 1d, four parcels orthogonally converge at the point H which is an extreme case from the horizontal circulation usually happened in strong typhoons and strong hurricanes with eyes for Category 4 or 5 tropical cyclones.

Assuming that the masses of four air parcels A, B, C, and D are m_A, m_B, m_C, and m_D and their moving velocities are v_A, v_B, v_C, and v_D at horizontal directions $\vec{n}_A$, $\vec{n}_B$, $\vec{n}_C$, and $\vec{n}_D$, respectively. Therefore, the kinetic energies of the four air parcels are $E_A = \frac{1}{2}m_A v_A^2$, $E_B = \frac{1}{2}m_B v_B^2$, $E_C = \frac{1}{2}m_C v_C^2$, and $E_D = \frac{1}{2}m_D v_D^2$. In four types from Fig. 1, air parcels undergo an arc-like bend before they converge to the point H. In the Northern Hemisphere, meso-scale vortexes and synoptic-scale cyclones are circled and converged by counterclockwise airflows because of the Coriolis Effect.

In most cases, the collision of two airflows has an angle like in Fig. 1c. The shear stress modulus reaches the maximum only when their angle between $\vec{n}_A$ and $\vec{n}_B$ is 90° ($\tau_H > 0$) or 270° ($\tau_H < 0$). The shear stress modulus is zero for the tailgating convergence in Fig. 1a and the head-on convergence in Fig. 1b.

The idea of this paper is to explain the downdraft of tornado and strong hurricane center as well as the updraft ring around them by orthogonal convergence of anomalous airflows. The physical decomposition of atmospheric variables and the orthogonal interaction of anomalous airflows are two basic approaches. The latter theory and method have been introduced and used in this paper. The climatology at a spatial point of the Earth's atmosphere varies with a daily 24-h cycle and an annual 365-day cycle as the altitude angle of the Sun changes. Hourly climatology can be estimated by averaging reanalysis data for a variable such as wind v, temperature T, and geopotential height H at time t (24 h a day) on calendar date d over M years,

$$\widetilde{v}_d(\lambda, \varphi, p, t) = \sum_{y=1}^{M} v_{(d,y)}(\lambda, \varphi, p, t) \Big/ M. \tag{6}$$

Where, year y runs from 1 to M ($M \geq 30$ years), while λ, φ, and p denote longitude, latitude. and pressure level, respectively. When M is large enough, the estimated climatology should physically be a static state under thermodynamic equilibrium of the Earth-atmosphere system, which is only forced by the solar radiation and surface conditions (Qian, 2017; Qian et al., 2021a). The hourly climatology contains the diurnal cycle and the annual cycle. Usually, reanalysis data are used with M = 30 years (1981–2010), which are available four times per day at 6-h intervals. Once the climatology is known, an anomaly $v'_{(d,y)}(\lambda, \varphi, p, t)$ can be extracted from a total variable $v_{(d,y)}(\lambda, \varphi, p, t)$ by subtracting the climatology $\widetilde{v}_d(\lambda, \varphi, p, t)$,

$$v_{(d,y)}(\lambda, \varphi, p, t) = \widetilde{v}_d(\lambda, \varphi, p, t) + v'_{(d,y)}(\lambda, \varphi, p, t). \tag{7}$$

Thus, the total, climatological and anomalous variables can be physically decomposed from Eq. (7).

The wind and other variables used in this analysis with spatial

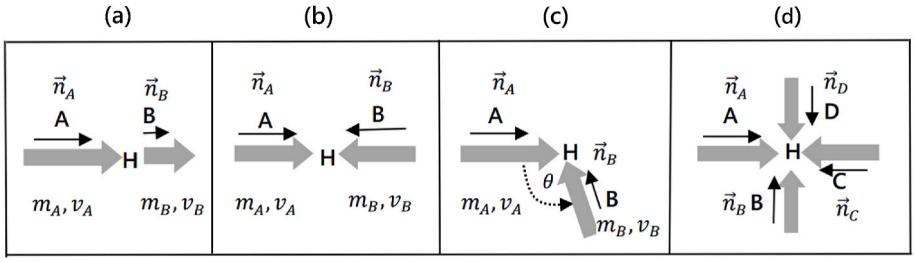

Fig. 1. Four schematic types of airflow convergence with their air masses and velocities such as air parcel mass m_A with velocity v_A. (a) *tailgating collision* that the parcel A is moving in $\vec{n}_A$ direction and the parcel B is moving slowly in the same direction; (b) *head-on collision* that the parcel A is moving in $\vec{n}_A$ direction and the parcel B is moving in $\vec{n}_B$ direction, where they converge toward each other head to head (or face-to-face); and (c) *cross convergence* that is the same as (b) but they are converging toward each other from an angle θ; (d) *orthogonal convergence* by four adjacent air parcels A, B, C, and D. The letter *H* indicates the convergence point.

resolution of 0.25 latitude-longitude degrees is download from the fifth generation ECMWF atmospheric reanalysis (ERA5) data. The side is at https://cds.climate.copernicus.eu/cdsapp#!/dataset/reanalysis-era5-pressure-levels. The formulas for calculating vorticity and divergence are the commonly used form by that the vorticity and divergence at a point require winds at four points around it. The calculation of total kinetic energy is directly using the square of anomalous wind velocity on a grid and taking the mass as 1. The shear stress modulus of anomalous winds is calculated using Eq. (4), taking the mass is 1 and considering the direction of the airflows on each point. When two airflows converge towards a point, the shear stress modulus needs to consider the angle between the two airflows. If the angle is less than 180°, the shear stress modulus is positive, otherwise, a negative if the angle is greater than 180°. The positive and negative values of the shear stress modulus separate the direction of shear stress at that point when one stands on a side. When the angle is 90° (or 270°), the shear stress modulus reaches the maximum (or the minimum). In fact, the shear stress has two opposite directions relative to the plane of two anomalous airflows.

3. Single tornado

In China and many parts of the world, tornado as individual vortex system occurs in a meso-scale cyclone (Qian et al., 2021b). The funnel-shaped vortex in Fig. 2a and b shows the downward motion of air under a rotated cumulonimbus cloud as understanding from Eq. (3) and Eq. (4). In Eq. (5), the orthogonal interactive energy $4E_AE_B$ of two air parcels concentrated at a unit area is the maximum energy density τ_{Hmax}. Also, there should be a strong ascending motion above the rotated cumulonimbus cloud with the high energy density, but it cannot be directly observed from Fig. 2a and b. When the funnel-shaped vortex with the high energy density sinks to the ground, it stirs up ground objects and soil or dust to spin up, forming a so-called the wall cloud (Rasmussen and Straka, 2007). The rotational directions of the inner funnel-shaped vortex (solid shadow in the center) and the outer wall cloud (surrounding shade of gray) are the same, but their overall directions of movement are vertically opposite.

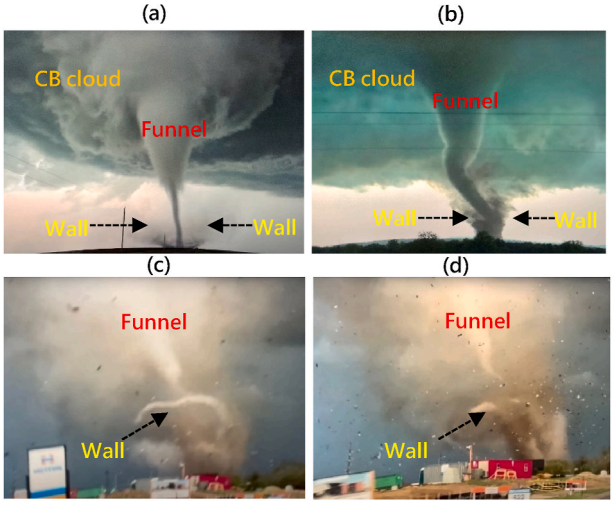

Fig. 2. Vertical structure of tornadoes. (a) and (b) are two tornado cases, inner funnel-shaped vortexes extended down from the bottom of cumulonimbus clouds while outer wall clouds rotated with rising dusts from the ground. (c) and (d) are another case of tornado, inner funnel-shaped vortex surrounded and rotated by rising debris (black or white dots) and dusts at two moments.

Fig. 2c and d are the relative distribution of inner funnel-shaped vortex and outer wall cloud of the same tornado at two moments. The gray-white swirling floating zone in the outer wall cloud is crushed matter from the ground. There are also debris flying around the outer wall cloud that follows the anomalous winds, indicating that the actual range of tornado damage is wider than that of the outer wall cloud. The outer wall cloud should be the result of the recoil action of the sinking funnel-shaped vortex relative to the ground.

Here, we give another example of environmental disturbance winds that occurred before a single tornado in the summer of 2023. At 15:58 Beijing Time (BJT) on 13 August 2023, a maximum wind velocity of 22.4 m/s (81 km/h) was observed at the site of the tornado in Yancheng City, Jiangsu Province, China. The tornado, which was scaled EF-2 in intensity and lasted for more than 10 min, traveled about 2.16 km, killed 2 and injured 15 people. Tornadoes mostly occur in the afternoon of summer because the ground surface temperature reaches its highest. In Fig. 3a, at 13:15 BJT, the ground surface temperature of Dongtai Station, 20 km southwest of the tornado site, reached a daily maximum of 62.1 °C, which was 14.8 °C higher than the ground surface temperature (47.3 °C) where the tornado occurred and 20.5 °C higher than that (41.6 °C) in the north of Yancheng. The anomalous temperature at Dongtai Station, which begins to increase since the morning, must cause anomalous airflows. At 12:00-13:00 BJT (Fig. 3b), there was a meso-scale anomalous cyclone *c* forming on the northwest side of Yancheng. At 13:00-14:00 BJT (Fig. 3c), the anomalous cyclone moved southeast to Yancheng. On the southwest side of the anomalous cyclone the airflows (two red arrows near the point L) are orthogonally converged, while the airflows (two red arrows near the point R) on the east sides are face-to-face (head-on) convergence.

In Fig. 3b and c, the observed winds around the meso-scale cyclone are equivalent to anomalous winds because climatological winds are small. Examples of anomalous winds near the surface with the orthogonal convergence to form a single tornado have also been respectively observed in Funing County, Jiangsu Province, China, on June 23, 2016 (Qian et al., 2017) and in Kaiyuan City, Liaoning Province, China, on 3 July 2019 (Qian et al., 2021b). The Funing tornado killed 99 people, which occurred at a place where the westerly and southerly anomalous winds orthogonally converged at 925-850 hPa. About 6–7 h prior to the Kaiyuan tornado, the orthogonal convergence of anomalous airflows was observed to follow the strong cloud image.

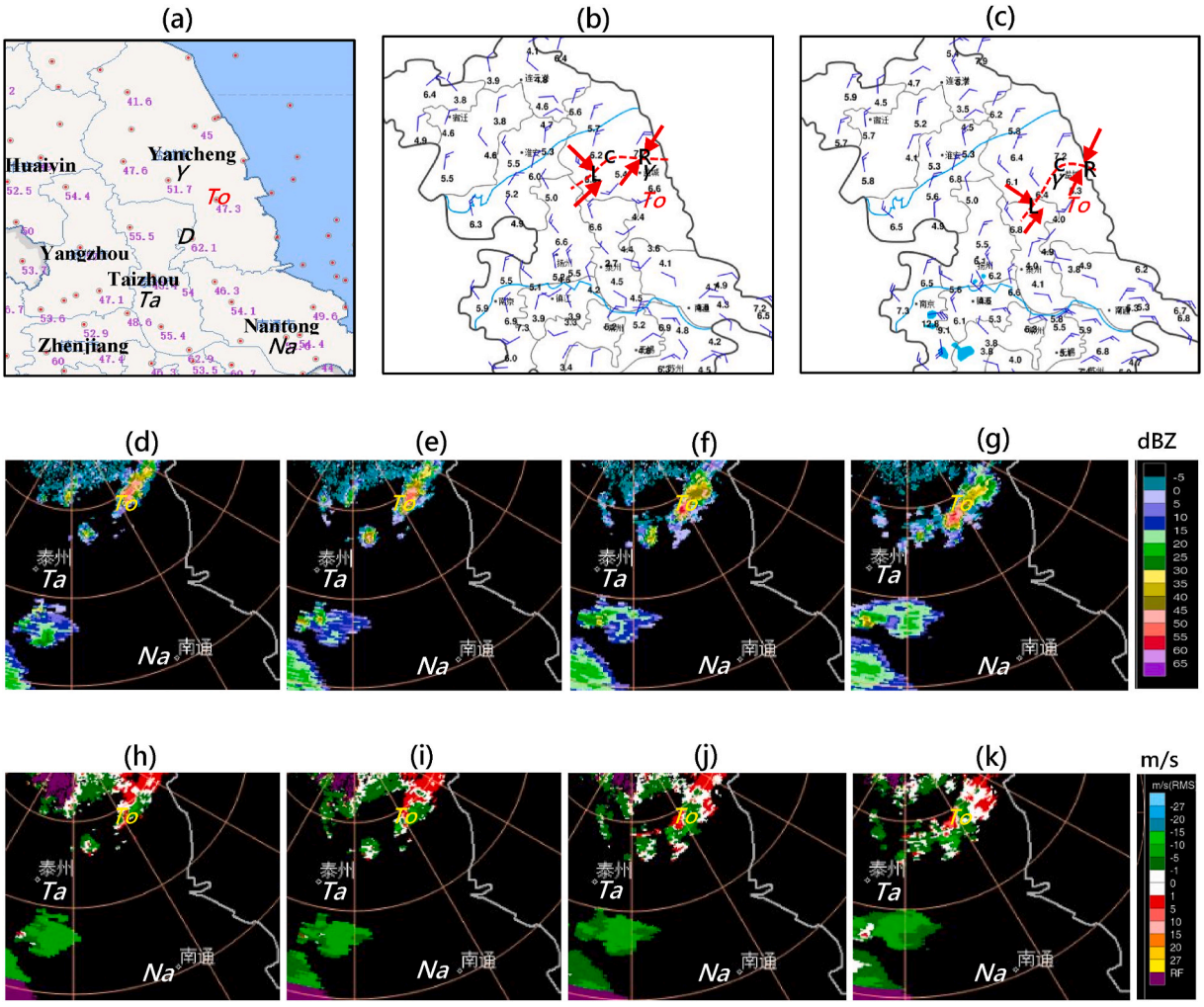

Fig. 3. Surface meteorological elements and radar echoes on the day of tornado in Yancheng City, Jiangsu Province, China, on August 13, 2023. (a) Surface temperature (pink digit, °C) at 13:15 BJT as well as maximum winds (direction and velocity of black digit, short barb = 2 m/s, long barb = 4 m/s) during each hour from (b) 12:00-13:00 BJT and (c) 13:00-14:00 BJT. The red arrow indicates the wind direction, while the red dashed line indicates the convergence line passing through the anomalous cyclone *c* and two points (L and R) in (b) and (c). Radar echo intensity (shading, 5 dBZ interval) at (d) 15:49, (e) 16:01, (f) 16:12, and (g) 16:24 BJT. Radial wind velocity (shading, 5 m/s interval) scanned from Yancheng radar station at (h) 15:49, (i) 16:01, (j) 16:12, and (k) 16:24 BJT. Letters *Y,D,Ta,Na* indicate stations of Yancheng, Dongtai, Taizhou and Nantong while the letter *To* indicates the tornado place. (For interpretation of the references to colour in this figure legend, the reader is referred to the Web version of this article.)

Fig. 3d–g shows the distributions of radar echo intensity scanned from Yancheng Station. From 15:49 to 16:24 BJT, the center of echo intensity at the site of tornado occurrence (marked by the yellow letter "*To*") reached 60–62 dBZ. In Fig. 3h-k, radial wind convergence line scanned at an altitude of 2.6 km can be identified between red and green shadings. It is also marked by the yellow letter "*To*" and located on the west side of the cyclone center (Fig. 3b-c). The centers of the strong radar echo and the radial wind convergence move from northeast to southwest, which coincides with the track of the tornado.

As shown in Fig. 3a-c, the occurrence of a tornado is the release of anomalous temperature internal energy and anomalous wind kinetic energy accumulated since the morning. Radar echo can monitor and track the location and intensity of high energy density formed by the convergence of anomalous airflows. This can be identified from Fig. 3d-g, in where the center of strong echoes and the tornado are associated with the convergence of anomalous airflows in Fig. 3h-k. Clearly, the high energy density and strong echoes are accompanied with the convergence of orthogonal anomalous airflows at the point L in Fig. 3b-c. However, low energy density and weak echoes are observed in the point R where the head-on convergence of anomalous airflows exists.

4. Tornado swarms

In the United States, tornadoes are mostly occurrence in groups within squall lines. For an example of the worst tornado outbreak days so far in this 21st century, multiple tornadoes occurred from west to east in the southern United States during 25–28 April 2011 (Knupp et al., 2014). The most severe tornado swarms occurred on 28 April 2011 (Qian et al., 2019). During a 6-h period centered at 00:00 UTC on 28 April 2011, multiple tornadoes formed from the north of Mississippi and Alabama to Tennessee and Kentucky (Fig. 4a–c). At the 925 hPa level of a traditional weather map (Fig. 4a), one low-pressure center is in Great Lakes, and another weak low-pressure center is in Kentucky. Heavy rainfall and multiple tornadoes associated with squall lines occurred in a weak warmer zone but located on the east side of the two height troughs. The systems on the conventional weather map cannot obviously indicate the tornadoes and squall lines or extreme rainfall because the climatological background component is contained in Fig. 4a. At this moment, the climatological temperature shows that the United States is warm in the southwest and cold in the northeast (Fig. 4b). In fact, extreme rainfall and tornadoes are difficult to be explained by the distribution of climatological temperature and height. In contrast, if the climatological

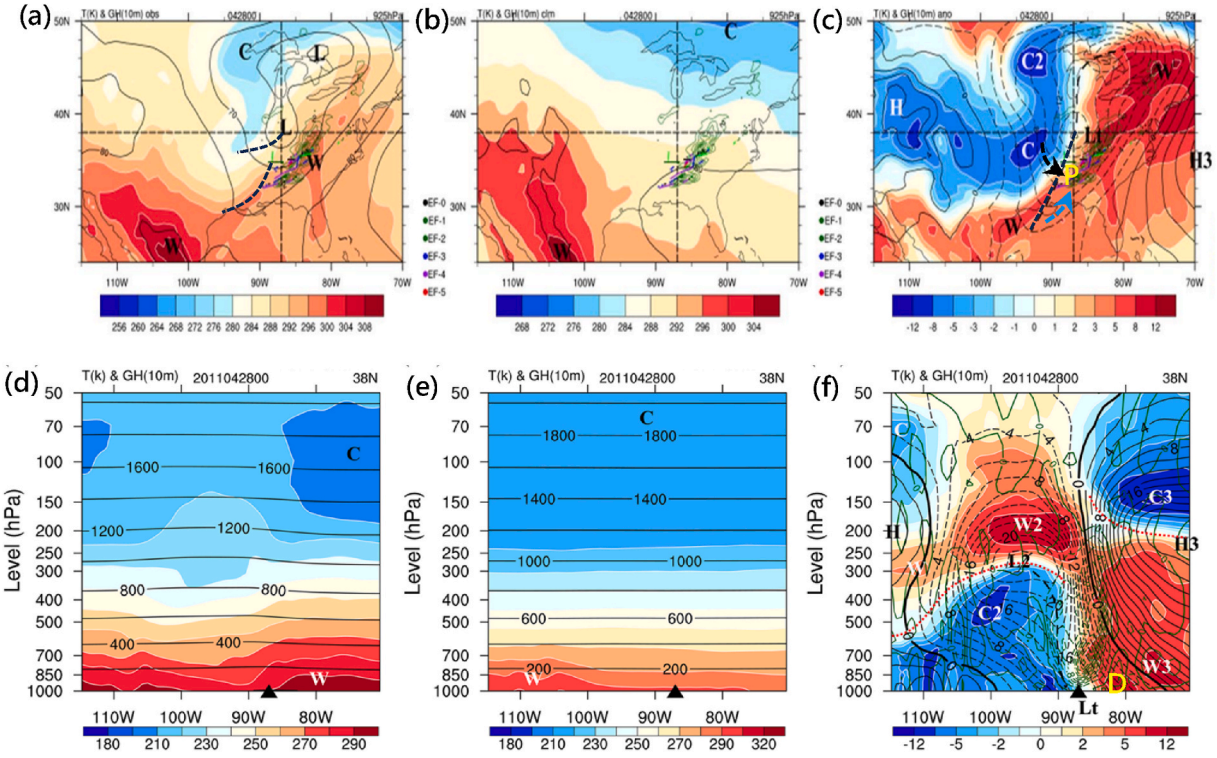

Fig. 4. Spatial distribution of variables at 00:00 UTC on 28 April 2011, modified from Qian et al. (2019). (a) Horizontal distributions of total height (contour, 5 × 10 gpm interval) and total temperature (shading, 4 K interval) at 925 hPa. (b) Same as (a) but for climatological height and climatological temperature. (c) Height anomalies (contours, 2 × 10 gpm interval) and temperature anomalies (shading, 1, 2, 3 and 4 K intervals). Green contour indicates the hourly precipitation rate (2.5 mm/h interval) and thick dashed lines denote the trough of height anomalies. Colored straight lines denote tornado tracks from EF-0 to EF-5 scales centered within 6 h. The black and blue arrows indicate anomalous winds orthogonally converged at the point *P* in (c). (d) Vertical distributions of total height (contour, 200 × 10 gpm interval) and total temperature (shading, 10 K interval) along 38°N. (e) Same as (d) but for climatological height and climatological temperature. (f) Height anomalies (contours, 2 × 10 gpm interval) and temperature anomalies (shading, 1, 1.5, and 3.5 K intervals). Letters "H/L" and "W/C" denote the centers of height and temperature (or anomalies). The triangle "▲" is the central position of the surface anomalous low (Lt), while the thick dashed line is the trough axis of height anomalies. The green solid and dashed contours, respectively, indicate anomalous sinking and rising pressure velocities (0.2 Pa/s interval) while the red-dot line is the zero line of temperature anomalies in (f). (For interpretation of the references to colour in this figure legend, the reader is referred to the Web version of this article.)

component (Fig. 4b) is subtracted from the total variable (Fig. 4a), the anomalous variable-based weather map (Fig. 4c) can clearly show that heavy rainfall and tornadoes occur in the anomalous warm zone on the east side of the anomalous height trough. According to the geostrophic wind and thermal wind relationships of anomalous variables (Qian et al., 2016a; Qian, 2017), we can calculate the spatial distribution of temperature anomaly and wind anomaly by using height anomaly. Based on the anomalous height contours, we can determine the orthogonal convergence point *p* of anomalous airflows indicated by the black and blue arrows. The heavy rainfall and tornadoes occur along the zone where two anomalous airflows orthogonally converged.

In Fig. 4c, the tornados occur to the east of the approximately north-south oriented anomalous height trough. Therefore, we plotted an east-west oriented vertical profile corresponding to Fig. 4a–c through the low-pressure center L1 (Fig. 4d–f). On the conventional weather map (Fig. 4d), there are horizontal weak fluctuations in the total height and strong fluctuations in the total temperature. The climatological height and temperature are shown in Fig. 4e. Fig. 4f is the anomaly part (i.e., Fig. 4d minus Fig. 4e). The anomaly apparently reveals detailed information. First, in the whole atmosphere from the troposphere to the stratosphere, there are four symmetrical anomalous warm-cold air masses above the tornado location. Near the tropopause, there are a positive center and a negative center of height anomalies. The positive center (H3) of height anomaly separates an anomalously warm mass (W3) below and an anomalously cold air mass (C3) above. In contrast, an anomalously cold air mass (C2) and an anomalously warm mass (W2) are located below and above the negative center (L2) of height anomaly, respectively. The symmetrical distribution of four cold-warm air masses reflects the presence of anomalous internal energies relative to the climatological field.

Fig. 4f shows that the release of potential anomalous internal energy in the whole atmosphere surrounding the low-pressure center (Lt) necessarily excites the anomalous kinetic energy. The strong contrast of the tropospheric anomaly cold and warm air masses will excite a strong anomaly upward movement over the low-pressure center. The ascent velocity zone in the troposphere spans 500–600 km horizontally and belongs to the synoptic-scale system. We note that there is a meso-scale downdraft (yellow D) in the lower troposphere (925-850 hPa) 400–500 km on the east of the ground low-pressure center (Lt). This meso-scale downdraft is corresponded to the orthogonal convergence of north-westerly and southwesterly airflows (two arrows) in Fig. 4c.

A tornado forms in a funnel-shaped vortex extending downward from the bottom of a cumulonimbus cloud (Fig. 2a) and Eq. (3). A cumulonimbus cloud is usually located at height of low-level jets, a few hundred to one thousand meters above the ground. In plain areas, this height corresponds to around 925 hPa (Fig. 4c and 2a). In Fig. 4c over a certain length from northeast to southwest through the point *p*, there is a zone of large shear stress modulus. Therefore, we can calculate the anomalous shear stress modulus using the anomalous winds at the 850–925 hPa layer to determine the location of heavy rainfall and tornado swarms associated with the squall lines. In Fig. 4f, the synoptic-scale anomalous system creates a background condition for multiple

tornado outbreaks. In Fig. 4c, multiple tornadoes occur on a cyclonic shear line where the anomalous horizontal airflows orthogonally converge (or collide) to create upward and downward motions.

In Fig. 4f, in addition to small- and meso-scale systems such as thunderstorms, squall lines, and tornadoes, it is also possible to analyze abnormal weather at the synoptic scale. Both the positive center (H3) and the negative center (L2) of height anomalies are located near the tropopause. According to the thermal wind relationship of the anomalous variables, we can calculate the spatial distribution of wind anomalies and temperature anomalies associated with height anomalies. As a result, a positive temperature anomaly occurs in the troposphere below the positive center of height anomalies. In Fig. 4f, the temperature anomaly near the ground reaches +12 °C. If such a vertical distribution of height anomalies occurs in summer, there are bound to be high temperatures and heat waves on the ground.

5. Strong tropical cyclones

Satellites can observe changes in the intensity and position of tropical cyclones' cloud images from high altitudes. In Fig. 5a, the appearance of an inner eye (shadow at E, sometimes it is a clear-sky eye) indicates that it is a strong hurricane with its Category 4 or 5. There is a white cloud ring around the inner eye of the hurricane, which is called the outflow cloud shield, or simply the outer cloud shield (Mathur, 1998). The outermost periphery of the strong hurricane has four spiral cloud-rain bands or four airflows (yellow dotted arrows) that rotate and converge toward the outer cloud shield (Fig. 5a). Four convergence airflows enter the outer cloud shield and continue toward the inner eye E, as indicated by the red and blue dashed arrows in Fig. 5b. Two airflows passing through points A and B collide orthogonally with two centripetal forces at the point E. Similarly, the two airflows passing through points C and D also collide orthogonally at the point E. The spiral cloud-rain band structure in Fig. 5 usually corresponds to strong typhoons or strong hurricanes in their intensity. What occurs at the point E is a continuous orthogonal collision (convergence) of four spiral airflows. The result of orthogonal collisions of horizontally converging airflows at the point E excites the downward and upward movements of new airflows as understanding from Eq. (3).

We use the Hurricane Sandy, which occurred in October 2012, as an example to illustrate the internal dynamics of a strong hurricane. Sandy's intensity and track were anomalies, causing severe disasters in the northeastern United States (Bassill, 2014; Burger and Gochfeld, 2014). Its central pressure reached the lowest 940 hPa at 1800 UTC on 29 October 2012 a few hours before its landfall (Qian et al., 2016b). The Sandy's initial peak in intensity occurred just before the landfall in Cuba on 25 October 2012. Similarly, as shown in Fig. 5, the Sandy's cloud structure of inner eye and outer cloud shield were clearly observed to have two peaks on 25 and 28–29 October 2012, respectively. Fig. 6 shows a comparison of total and anomalous variables from the vertical and horizontal distributions crossing the Sandy center at the second peak time. Some weak and strong fluctuations can be observed from the vertical profiles of total height and total temperature (Fig. 6a). Fig. 6b shows the spatial structure of height anomalies and temperature anomalies after the removal of the climatological height and climatological temperature from the total variables. The hurricane's anomalous low pressure (L0) is in the troposphere and extends vertically up to 300 hPa. Its warm core (W0) is in the troposphere. To the southwest of the hurricane center, there is a negative center (L4) of height anomalies at the tropopause with a warm air mass (W4) above in the stratosphere and a cold air mass (C4) below in the troposphere. In areas controlled by anomalous cold air mass (C4), there were cold surge and 30–91 cm of snowfall on 28 October 2012 over West Virginia's 55 counties. To the northeast of the hurricane center, there is a positive center (H3) of height anomalies on 150 hPa with a cold air mass (C3) above and a warm air mass (W3) below.

In Fig. 6b, according to the relationship between thermal wind and geostrophic wind, high temperature anomalies (W3 and W0) form between the positive height anomaly (H3) and the negative height anomaly (L0) in the troposphere. The low temperature anomaly (C4) and the high temperature anomaly (W4) form below and above the negative height anomaly center (L4). According to the thermal-wind relationship, the thermal imbalance of temperature anomalies in Fig. 6b will lead to the dynamic imbalance inside the hurricane. In the troposphere, the updraft (green dashed lines) located in the southwest of the hurricane center should be produced by the strong contrast between the warm air masses (W3+W0) and the cold air mass (C4) in the troposphere. The maximum gradient of height anomalies appears in the troposphere where the gradient at 300 hPa (Fig. 6c) is larger than that at 850 hPa (Fig. 6d). Thus, the convergence of anomalous winds at the upper troposphere is larger than that at the lower. It means that the maximum shear stress should appear at the upper troposphere around 300 hPa and forms strong downward motion (green solid lines) at the center of the hurricane. The divergent layer will be raised to a height above 200 hPa. Due to the interaction with other nearby anomalous systems, the hurricane eye and cloud shield are no longer vertically symmetrical. However, height anomaly, temperature anomaly, and wind anomaly still satisfy the intrinsic dynamic relationship.

There are interactions of airflows in various scales in the Earth's atmosphere. The largest one is the interaction of planetary-scale airflows, formed by the Hadley cell, the Ferrel cell, and the Polar cell in

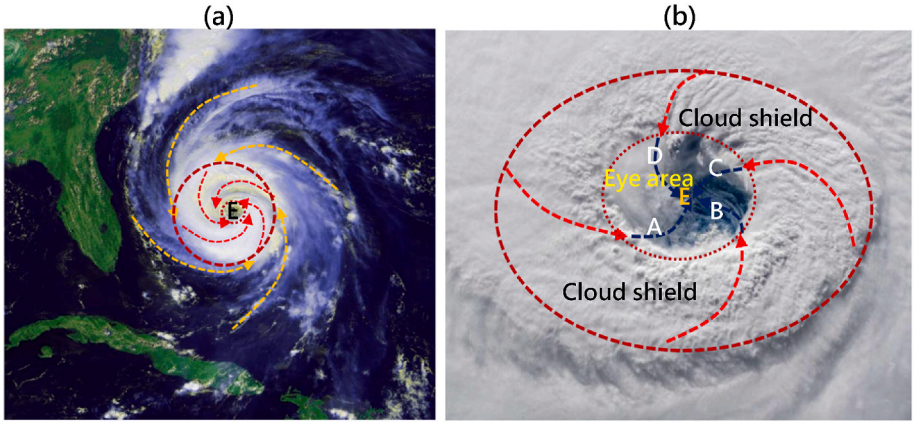

Fig. 5. Horizontal structure of strong hurricane cloud image. (a) The outer cloud shield (white shaded ring with four red-dotted line arrows) around the inner eye (E, central shadow) of hurricane and four spiral cloud-rain bands (yellow dashed-line arrow) around the periphery. (b) An inner eye (E) surrounded by the outer cloud shield between the red-dotted circle line and the red-dashed circle line. Red and blue dashed arrows indicate the convergence spiral airflows in (b). (For interpretation of the references to colour in this figure legend, the reader is referred to the Web version of this article.)

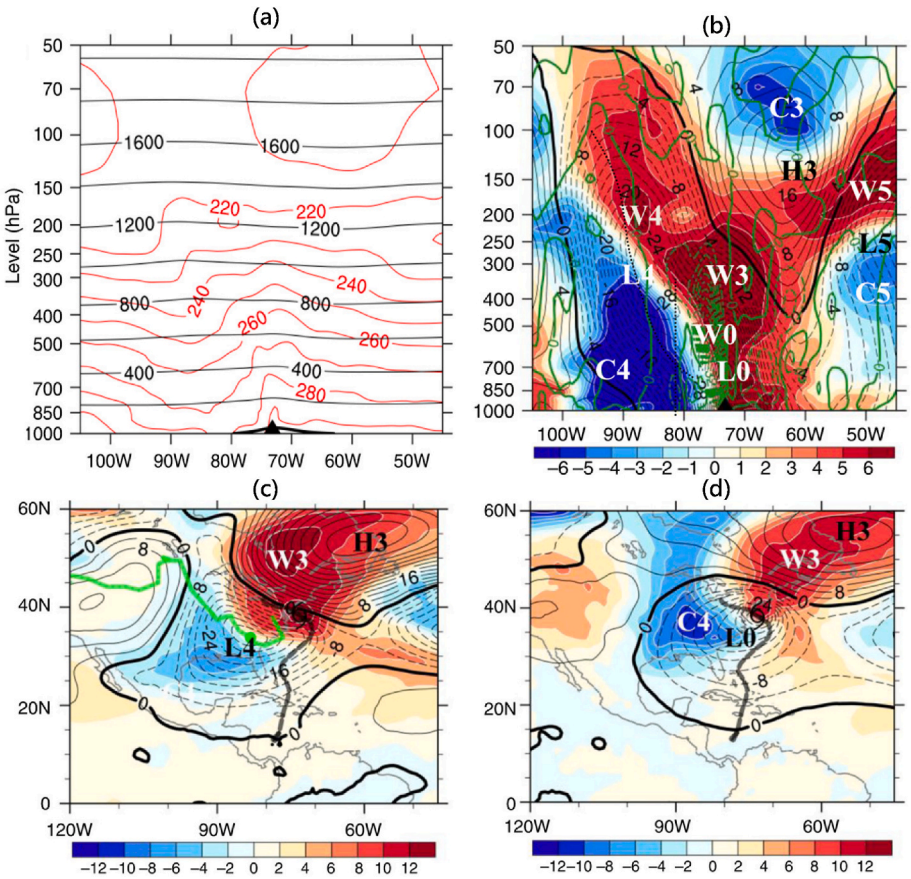

Fig. 6. The spatial structure of the Hurricane Sandy at 18:00 UTC on 29 October 2012, modified from Qian et al. (2016b). (a) Vertical total height (black solid line, 200 × 10 gpm interval), and total temperature (red solid line, 10 K interval) along 38.25°N. (b) Same as (a) except of height anomalies (black solid and dashed lines, 2 × 10 gpm interval) and temperature anomalies (shading, 1 K interval). In (b), the green solid and dashed lines, respectively, indicate anomalous descending and rising pressure velocities (10 hPa/s interval). Height anomalies (thin solid and dashed lines, 4 × 10 gpm interval) and temperature anomalies (shading, 2 K interval) at (c) 300 hPa and (d) 850 hPa. In (c) and (d), the thick green line is the track of anomalous vortex (L4) and the thick black line is the best track of Sandy. Letters "H/L" and "W/C" indicate the positive/negative centers of height anomalies and temperature anomalies. (For interpretation of the references to colour in this figure legend, the reader is referred to the Web version of this article.)

each hemisphere (Liu, 2021). At low latitudes, there are the basin-scale Walker cell in the troposphere on the east-west oriented vertical profile (Han et al., 2017). In addition, tropical cyclones with planetary-scale cloud-rain bands are associated with the so-called the inter-tropical convergence zone (ITCZ) (Barry and Chorley, 1992). The formation of ITCZ is directly linked with the two tropical Hadley cells. Between the Ferrel cell and the Polar cell in each hemisphere, there is a polar frontal convergence zone with the activity of extratropical cyclones and precipitation (Yoshino, 1968).

The ITCZ in the lower troposphere is clearly formed in the Pacific by the convergence of the northeasterly trade wind from the Northern Hemisphere and the southeasterly trade wind from the Southern Hemisphere. An important phenomenon shows that the northeasterly airflows and the southeasterly airflows converge orthogonally with an angle of near 90° along the ITCZ. Sometimes, several tropical cyclones formed along the ITCZ are influenced by this type of airflow convergence. Fig. 7b shows the ITCZ (red dashed line) derived from 850 hPa reanalysis (ERA5) total winds at 18:00 UTC on 14 July 2020. We will examine the relationship between satellite cloud image and three physical parameters of anomalous winds.

There are two types of meteorological satellites, the polar-orbiting satellites, and geostationary satellites. The latter is located above the equator and can continuously observe cloud systems within a certain range below the satellite. The polar-orbiting satellite orbits the Earth's north and south poles at relatively low altitudes, and the resolution of observations is high, but its observed cloud images are separated by a longitude band as shown in Fig. 7a around 18:00 UTC on 2 June 2021. The cloud image is the observed result of four times circled the poles. There are four narrow black bands without observations. The four cloud system positions (C1–C4) and four cloudless positions (A1-A4) are respectively located on the two sides of the ITCZ.

We calculate the shear stress of the anomalous winds using the lower atmospheric airflows at the corresponding time and investigate the ability to indicate the cloud systems in Fig. 7a. The shadow in Fig. 7b is the shear stress modulus calculated from the anomalous winds using Eq. (4). Four wave-like shading areas along the ITCZ are the shear stress modulus generated by the collision of the anomalous airflows. The ITCZ is well outlined the north boundary from both of cloud systems (tropical cyclones) in Fig. 7a and shear stress modulus (shading areas) in Fig. 7b. The four large centers of shear stress modulus in Fig. 7b calculated from the anomalous winds correspond to the four cloud systems observed by the satellite in Fig. 7a.

The shear stress modulus was also used in the study of wave-like uplift plateau in Southern Asia during the early Earth's geological evolution (Qian et al., 2023). Three plateaus (the Tibetan Plateau, the Iranian Plateau, and the Armenian Plateau) in Southern Asia are along the upper magma fluid ITCZ which is similar as the tropical anti-cyclones (A1-A4) formed along the atmospheric ITCZ in Fig. 7a and b. In Fig. 7c, the total kinetic energy of anomalous winds can also indicate four tropical cyclones (C1–C4), but it cannot indicate the directions of vertical movement at this pressure level. In Fig. 7d, the positive vorticity of anomalous winds can partially indicate where these cyclones are

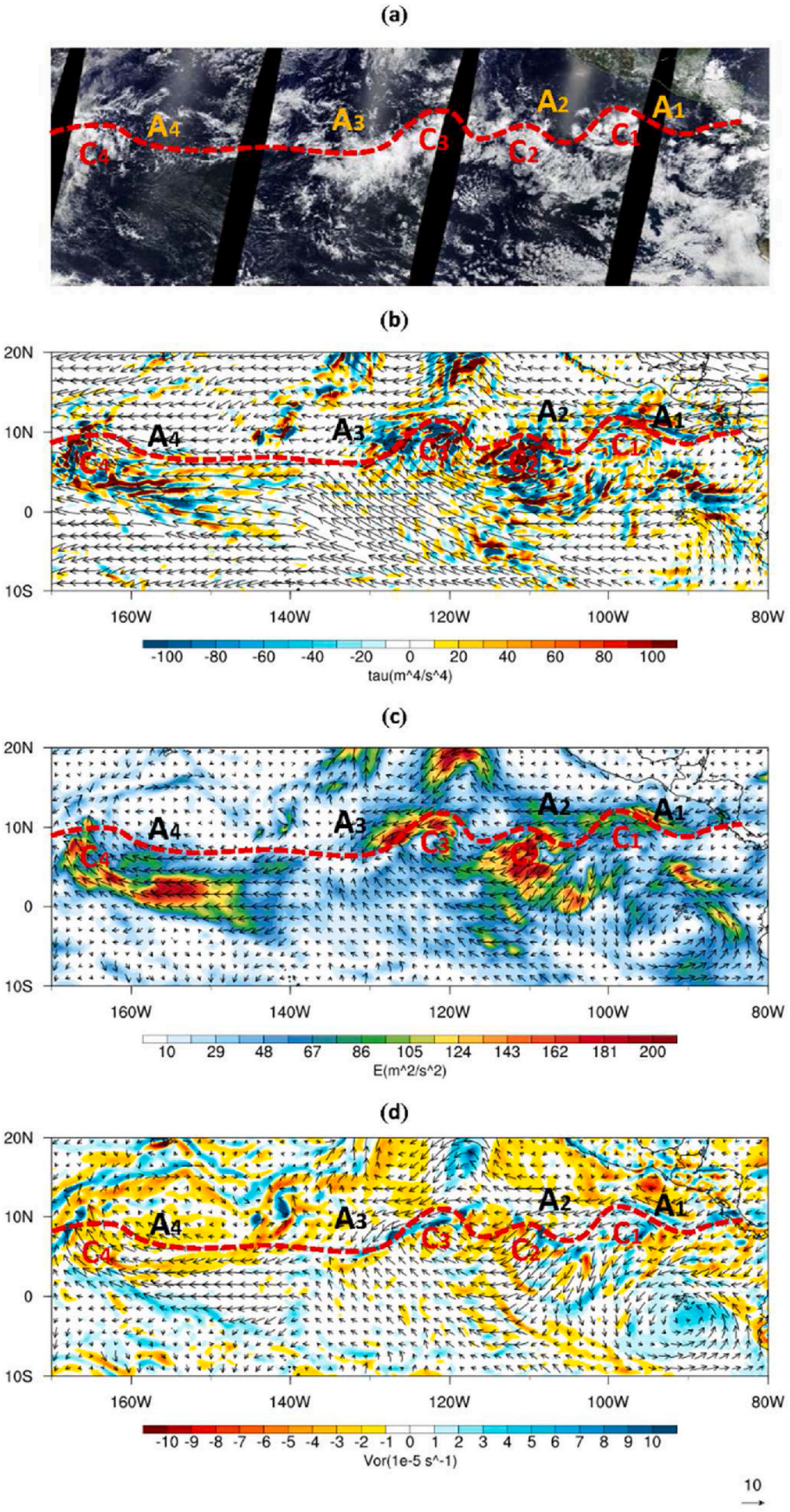

(caption on next page)

Fig. 7. (a) Satellite cloud image and three physical parameters derived from 850 hPa anomalous winds at 18:00 UTC on 14 July 2020. (b) Reanalysis (ERA5) total wind (arrow, m/s) and shear stress modulus (shading, 10 m^4/s^4 interval). (c) Total kinetic energy (anomalous wind arrow, shading, 19/2 m^2/s^2 interval). (d) Vorticity (anomalous wind arrow, shading, 1 × 10^{-5}/s interval). The red dashed line indicates the inter-tropical convergence zone (ITCZ) of total winds at 850 hPa. The letters C and A respectively indicate the center of tropical cyclone and anti-cyclone along the ITCZ. (For interpretation of the references to colour in this figure legend, the reader is referred to the Web version of this article.)

located because negative vorticities exist in anti-cyclones. Total winds and anomalous winds are different when comparing Fig. 7b and c. The anomalous weather indicated by cloud clusters (Fig. 7a) is associated with anomalous winds or anomalous total kinetic energy (Fig. 7c).

Fig. 8 is another example of a cloud image and the shear stress modulus of anomalous winds comparing with divergence of anomalous winds at 18:00 UTC on 30 May 2021. In Fig. 8a, there are three cloud systems (C1–C3) located on the south side of the red dashed line, while on the north side there are two cloudless areas (A1-A2). The red dashed line is the ITCZ based on the reanalysis (ERA5) total winds at 18:00 UTC on 30 May 2021. Three anomalous cyclones are clearly indicated by the three shading areas of shear stress modulus that is calculated from the anomalous winds. Critically, the three centers of shear stress modulus in Fig. 8b provide a good indication of the three cloud systems observed by the satellite in Fig. 8a. The total kinetic energy in Fig. 8c can well indicate the locations of three tropical cyclones, while the divergence field of anomalous winds in Fig. 8d cannot indicate the three tropical cyclones.

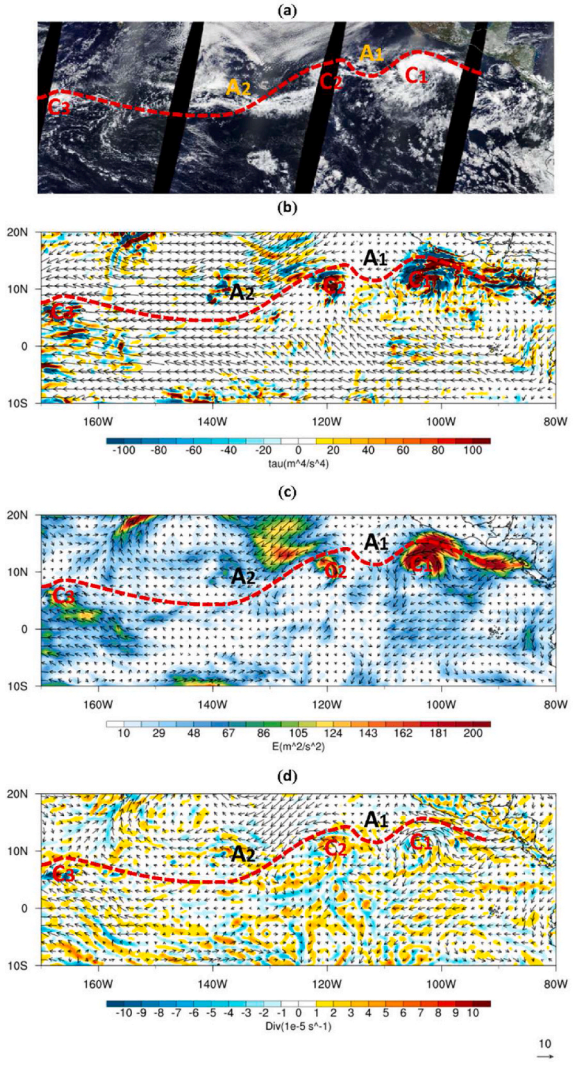

Fig. 8. Same as Fig.7 but for a different case. (a) Satellite image, (b) shear stress modulus, (c) total kinetic energy, and (d) divergence (anomalous wind arrow, shading, 1 × 10^{-5}/s interval) at 18:00 UTC on 30 May 2021.

6. Extratropical cyclone and dust storm

The second largest interaction of airflows is associated with continental-scale land-sea distributions and mountain ranges. Fig. 9 shows the two types of convergence in continental-scale or regional-scale interactions of airflows. One type of convergence in Fig. 9 is the South China Sea monsoon trough (dotted line) formed by the south-westerly warm-wet monsoon airflows from the Indian Ocean and the southeasterly warm-wet monsoon airflows from the southwest edge of the subtropical high in the northwest Pacific (Yuan and Qie, 2008). A large amount of water vapor and heat is orthogonally converged by the two monsoon airflows to the South China Sea, forming the outbreak of the South China Sea monsoon and the generation of continuous precipitation. Another type of regional-scale airflow convergence is the subtropical monsoon trough (dashed line) formed by warm-wet south-westerly airflows from the western edge of the subtropical high in the northwest Pacific and the dry-cold northwesterly airflows from the north side of the Tibetan Plateau, from East China to the south of Japan (Fig. 9) (Wang et al., 2006). The thermodynamic-dynamic property of the subtropical monsoon trough is different from that of the South China Sea monsoon trough. The former shows the baroclinic feature, while the latter is barotropic. But they are all formed by the orthogonal convergence of two airflows.

In eastern China there is the seasonally moving convergence line formed orthogonally by the northwesterly dry-cold airflows traveling from the north side of Tibetan Plateau and the southwesterly warm-wet airflows from the south side of the Plateau (Ding and Chan, 2005). This seasonally moving convergence line during each boreal summer over eastern China is called as the Mei-yu front (Liu et al., 2003). Its thermodynamic-dynamic property is the same as that of the subtropical monsoon trough. These regional-scale convergence systems are mainly rain producers in East Asia (Hu et al., 2013; Pan et al., 2021). All anomalous lows or anomalous convergence systems shown in Fig. 9 or along the seasonally moving convergence line in eastern China can be well depicted by both satellite images and shear stress modulus of anomalous winds at the lower troposphere.

The above orthogonal interaction of planetary scale and continental scale airflows along these convergence lines can form persistent anomalous climate events. Every day in the world, most extreme disasters are caused by low-pressure systems such as tropical and extratropical cyclones. Fig. 10 is a real case which shows NOAA GOES-West satellite image for the northern California winter storm on 4 January 2023. It brought excessive precipitation (heavy rainfall and snow) and strong wind to the west coast of USA especially the northern California. An anomalous occluded cyclone centered at the point L is clearly visible from the 1000 hPa analysis winds over the Northeast Pacific (Fig. 10a). Three points A, B and C show the orthogonal convergence of different airflows in the occluded cyclone (Fig. 10b). The point A along the cold front is the place where the cold-dry northwesterly airflows (blue arrow) converge orthogonally with the warm-wet southwesterly airflows (red arrow). The point B along the warm front is the place where the warm-wet southwesterly airflows (red arrow) converge orthogonally with the warm-wet southeasterly airflows (purple arrow). The point C along the occluded front is the place where the cold-dry southwesterly airflows

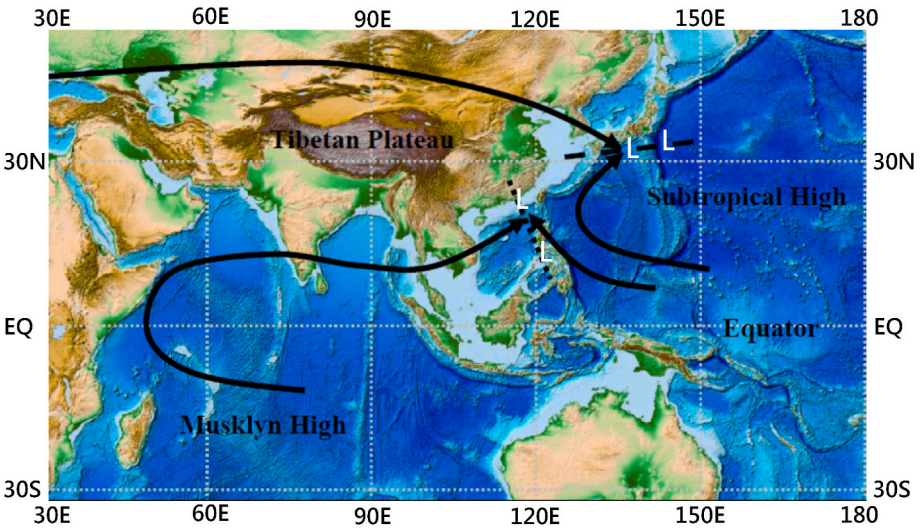

Fig. 9. Schematic diagram of East Asian airflow convergence lines interacted orthogonally by two airflows (heavy black arrow) in the lower troposphere. The dotted line indicates the South China Sea monsoon trough, and the dashed line is subtropical monsoon trough from the East China Sea to the south of Japan. The letter L indicates anomalous lows or anomalous convergence systems.

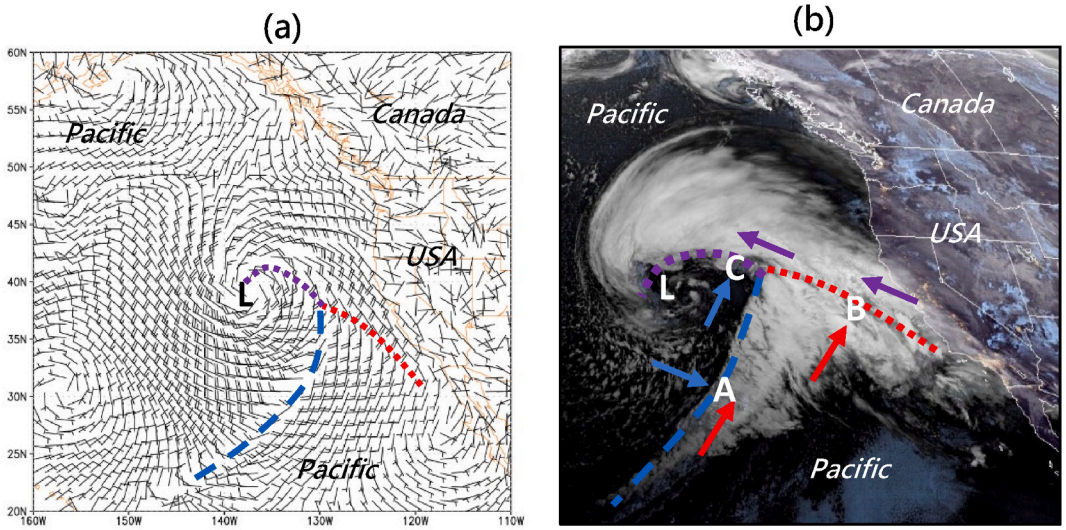

Fig. 10. The extratropical cyclone on 4 January 2023. (a) Wind direction and wind velocity (short barb = 5 m/s, long barb = 10 m/s, flag = 50 m/s) based on NCEP 1 000 hPa GFS analysis at 12:00 UTC. (b) The NOAA GOES-West satellite image at 12:20 UTC, which was associated with the northern California rainstorm caused by an occluded cyclone centered at L moving eastward. The blue dashed line, the red dotted line and the purple dotted line are cold, warm, and occluded fronts, respectively. Three letters A, B and C indicate three convergence points of airflows. The red, blue, and purple arrows respectively indicate warm-wet, cold-dry, and warm-wet airflows. (For interpretation of the references to colour in this figure legend, the reader is referred to the Web version of this article.)

(blue arrow) converge orthogonally with the warm-wet southeasterly airflows (purple arrow). Thus, heavy rainfall occurred at the place where different cold-warm or dry-wet airflows orthogonally interact with each other.

As an extratropical occluded cyclone, Fig. 11 gives the distribution of four physical parameters calculated by using the anomalous winds at 925 hPa level at 12:00 UTC on 4 January 2023. The positive vorticity is locally in the center of the occluded cyclone with a positive vorticity line extending along the shear line of total winds (Fig. 11a). In the occluded cyclone, there is a negative divergence line extending along the shear line of total winds (Fig. 11b). The total kinetic energy shows a large-value distribution of half circle except for the south part. The above three parameters cannot well indicate the rain-cloud distribution surrounding the occluded cyclone in Fig. 10b. In Fig. 11d, however, the center (L) is like an eye of strong tropical cyclone that is surrounded by the shear stress modulus. Warm front, cold front and occluded front are all clearly indicated by the adjacent positive and negative shear stress modulus. Distribution shape of the shear stress modulus in Fig. 11d is consistent with that of the cloud-rain image in Fig. 10b. In both tropical and extratropical cyclones, ascending and descending airflow bands and cloud-rain bands are commonly present.

Differing from the case in Figs. 10 and 11 that were cyclones over open ocean (northeastern Pacific), Fig. 12c and d show the case that a cyclone was formed and moved southeastward in the northeast Asian continent. Over the inner continent, there are less water vapor but a lot of dry sands on the ground. Strong surface winds can blow up dry sands, creating dust storm or airborne dust matter. The dust storm is another type of extreme weather (Lee and Kim, 2012; Qian et al., 2022) and associated with the release of anomalous energy which can be calculated using anomalous winds or anomalous airflows (Qian et al., 2021a). An example of dust storm is given in Fig. 12, which originated in Mongolia and moved southeastward into northern China during 14–15 April 2021.

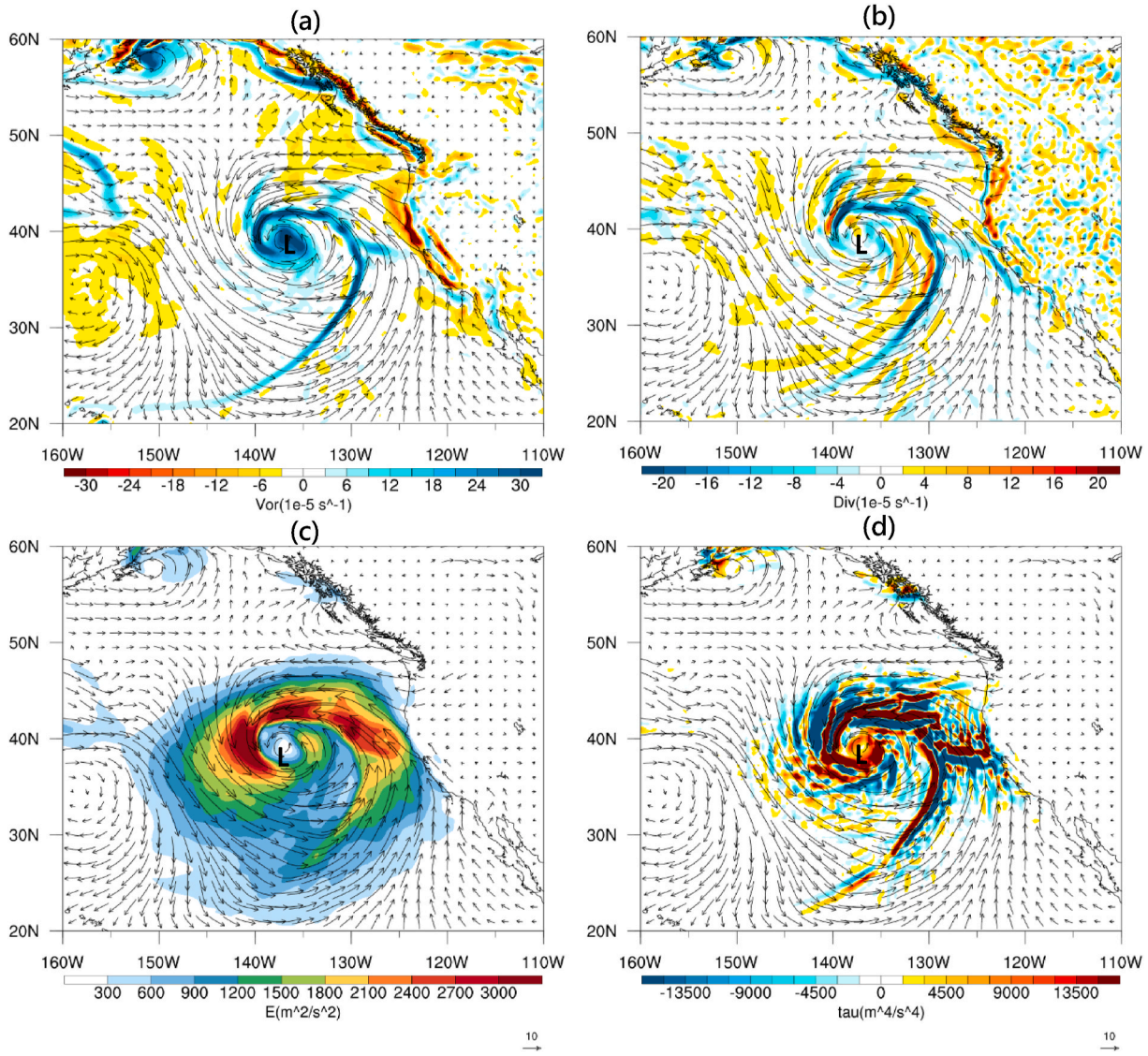

Fig. 11. Four physical parameters and total winds (m/s) of extratropical cyclone at 12:00 UTC on 4 January 2023 at 925 hPa level. (a) Vorticity (shading, 3×10^{-5}/s interval), (b) divergence (shading, 2×10^{-5}/s interval), (c) total kinetic energy (shading, 300 m^2/s^2 interval), and (d) shear stress modulus (shading, 1 500 m^4/s^4 interval).

Fig. 12a shows the spatial distribution of airborne dust matter detected by Japanese geostationary satellites at 20:10 BJT. The main body of airborne dust matter (red shading) was in the south-central part of Mongolia and a small portion has entered Inner Mongolia in northern China and even northwest of Gansu Province. The observed PM_{10} concentration of surface air volume exceeds 500 μg/ m^3 and the dust-air thickness can reach tens to hundreds of meters. The entry of such huge amount of airborne dust matter into the atmosphere indicates a high possession of kinetic and potential energies.

The concentration of airborne dust matter is the remote sensing data obtained from the Himawari-8 geostationary meteorological satellite of Japan Meteorological Agency (JMA). For this data, a new algorithm for dust detection was developed using brightness temperatures (BT) of infra-red (IR) channels to detect dust over land and ocean in both day and night (Martínez et al., 2009; Yamamoto, 2016). In Fig. 12b, the area of Mongolia within the yellow dotted area is covered by clouds, but airborne dust (red shading) can still be detected by the satellite in gaps that are not covered by clouds.

For almost all dust storm processes, a difficulty is determining the extent and movement position of dust storms such as in Fig. 12a and b and other cases (Qian et al., 2022). The reason is that the total variables of model products and traditional physical parameters are used in the daily operation of weather forecasting. Fig. 12c shows the distribution of atmospheric anomalous winds (airflows) at 850 hPa at 20:00 BJT on 14 April 2021. The anomalous winds are obtained by subtracting climatological winds from total winds at a given moment. An anomalous cyclone center was in the southeastern part of Mongolia. A shear line between an anomalous northerly airflow and an anomalous westerly airflow can be drawn on the west side of the cyclone center. The anomalous airflows on both sides of the shear line are interacting orthogonally with each other. This orthogonal interaction could be a mechanism to provide kinetic energy and lifting force for sand initiation (see Section 2).

In Fig. 12a, the yellow dashed line covered the dust storm. Its north side dashed line is the northern boundary of the dust storm, consistent with the shear line position of the orthogonal interaction of anomalous airflows (Fig. 12c). The northern boundary of the dust storm is flanked by the anomalous northeasterly airflows and anomalous northwesterly airflows. The anomalous airflows in the area covered by the dust storm were an anomalous westerly wind, indicating that the dust storm tends to move eastward as whole. The southern boundary of the dust storm (Fig. 12a) corresponds to the convergence line of anomalous westerly

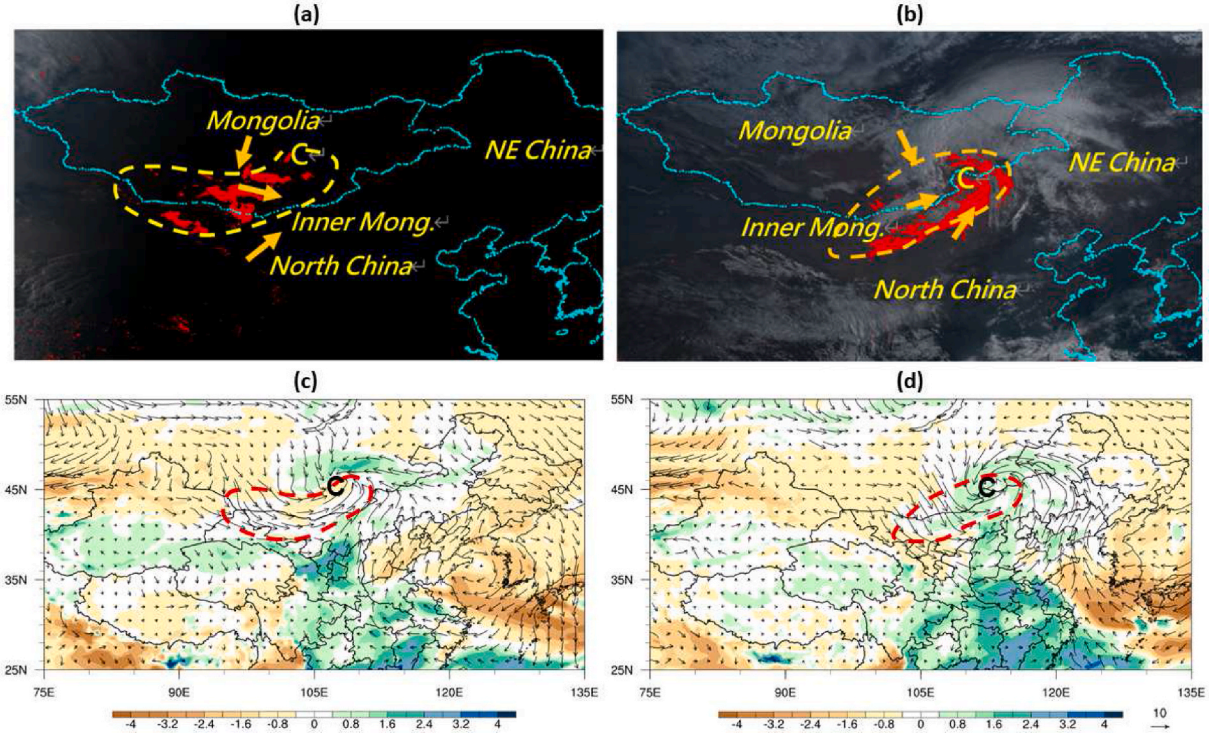

Fig. 12. Airborne dust matter (red shading) and cloud (gray, daytime) indicated by the Himawari-8 geostationary meteorological satellite of Japan Meteorological Agency at (a) 20:10 BJT on 14 and (b) 08:10 BJT on 15 April 2021 with the yellow dashed line indicating the outside boundary of dust matter. The letter C denotes the cyclonic center composed by dust matter and cloud in (a) and (b). The anomalous airflows (vector) and specific humidity anomalies (shading, 0.4×10^{-3} g/kg interval) at 850 hPa at (c) 20:00 BJT on 14 and (d) 08:00 BJT on 15 April 2021 are derived from the reanalysis (ERA5) data. In (a) and (b), yellow arrows indicate the directions of anomalous airflows. The letter C in four panels indicates the center of anomalous cyclone. In (c) and (d), the red dashed line indicates the shear line of anomalous airflows. (For interpretation of the references to colour in this figure legend, the reader is referred to the Web version of this article.)

and southwesterly airflows at 850 hPa (Fig. 12c). Thus, the boundary of a dust storm can be well enveloped by using anomalous winds as indicated by the red dashed line in Fig. 12c but not total winds.

After 12 h, the satellite image of dust storm showed like a cyclonic structure in Fig. 12b. The dust concentration has further increased, and the location has been moved to Inner Mongolia in China. At that time, the intensity and location of the dust storm are mostly controlled by the anomalous cyclone in Fig. 12d. The northern boundary of the dust storm lies exactly on the orthogonal interaction line between the anomalous northwesterly and southwesterly airflows. The southern boundary of the sandstorm is along the confluence line between the anomalous westerly and southwesterly airflows. Thus, the boundary of a dust storm can also be well enveloped by using anomalous winds as indicated by the red dashed line in Fig. 12d but not total winds.

On this case, the orthogonal convergence of two anomalous airflows is roughly the basic cause for the airborne dust matter uplifting from the sand ground. For more detail, the observed time series of PM_{10} concentration during the periods of six dust storms in spring 2021 at Peking University atmospheric observation platform showed large fluctuations (Qian et al., 2022). During the first case period, three main fluctuations of dust concentration were recorded from 15 to 17 March 2021 with their amplitude difference between two peaks about 400 μg/m^3. This hourly wave-like concentration bands can also be observed in Fig. 12a and b. Up to now, no one can answer this fluctuation in dust intensity. We found that numerical products produced by the ECMWF model can indicate the anomalous wind pattern with lead times of 4–8 days by applying the anomaly-based analysis approach (Qian et al., 2022). However, daily forecasting is unable to correctly indicate the coverage and wave-like concentration bands in hourly intensity based on the total variables.

Airborne dust concentration in the atmosphere is directly associated with wind strength at the lower layer except of dust source. Several indicators or physical parameters are used in diagnostic place to see whether they can be used to indicate the domain of dust storms. In Fig. 12c and d, specific humidity anomalies are not an effective indicator for the domain of dust storm. The dynamic mechanism of sand initiation is related to winds near the ground. As anomalous weather, we need to use anomalous winds. In Fig. 12c and d, the anomalous winds can roughly indicate the location of the occurrence of dust storms, but it is difficult to explain the wave-like characteristics of the spatial distribution of airborne dust concentration in Fig. 12a and b from the mechanism. Therefore, we calculate four physical quantities by using the anomalous winds, which are anomalous vorticity, anomalous divergence, total kinetic energy of anomalous winds, and shear stress modulus of anomalous winds.

The wind used here is from the reanalysis (ERA5) data at 850 hPa at 20:00 BJT on 14 April 2021 and at 08:00 BJT on 15 April 2021. In Fig. 13, the red dashed line surrounds the area of the dust storm. In Fig. 13a, positive and negative vorticities are scattered in the mid-latitude region from Xinjiang to Mongolia and Northeast China. In the area where dust occurs, positive vorticity is dominant. In addition, there is a pair of positive and negative vorticity zones in Northeast China but where is no airborne dust matter in Fig. 12a. In Fig. 13b, positive and negative divergences are distributed in the region of dust storm. The

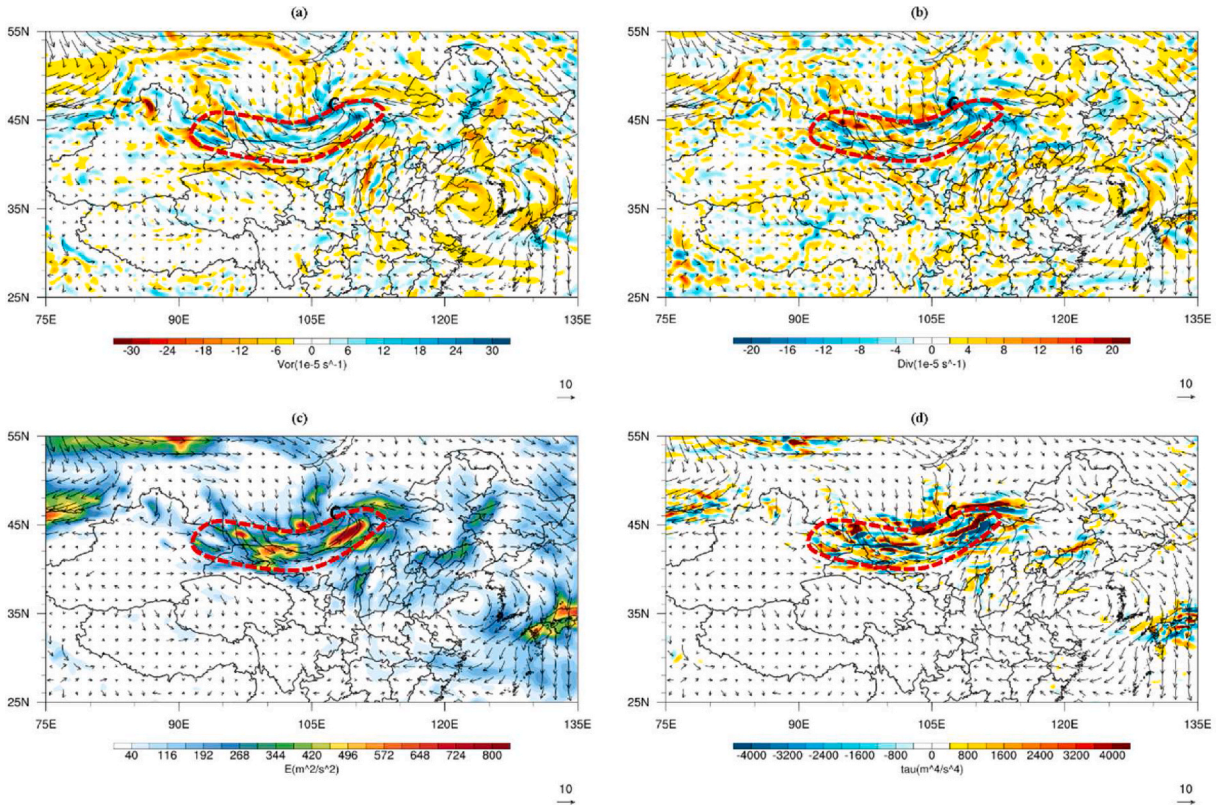

Fig. 13. Anomalous parameters derived from 850 hPa wind anomalies at 20:00 BJT on 14 April 2021. (a) Vorticity (shading, 3×10^{-5}/s interval), (b) divergence (shading, 2×10^{-5}/s interval), (c) total kinetic energy (shading, 38 m^2/s^2 interval), and (d) shear stress modulus (shading, 400 m^4/s^4 interval). The red dashed line covers the domain of dust storm, and the letter C is the center of anomalous cyclone. (For interpretation of the references to colour in this figure legend, the reader is referred to the Web version of this article.)

vicinity of cyclonic center is dominated by convergence (negative divergence). However, there are also positive and negative distributions of divergence elsewhere.

Fig. 13c has four general regions with large total kinetic energy distributions, one at the location of the dust storm and other three in Russia, west of Xinjiang and Japan. The total kinetic energy is always positive. There are two high-value centers of total kinetic energy in the dust storm region. Since Mongolia is the main source of sand, the high distribution area of total kinetic energy can indicate the range of dust storms, but it is difficult to explain the fluctuation characteristics of the spatial and temporal distributions of airborne dust concentration. Fig. 13d shows the spatial distribution of the shear stress modulus which can well indicate the dust storm. Except in dust storm, the shear stress modulus in the surrounding area is very weak or can be clearly comparable. A key feature is that the spatial distribution of dust concentration bands in Fig. 12a can be explained by the positive and negative band distribution of the shear stress modulus in Fig. 13d.

We specifically explain the significance of the positive and negative bands of the shear stress modulus in Fig. 13d. In Eq. (3), the shear stress has two directions, pointing to the upward sky and the downward ground. The occurrence of extreme weather is all related to strong vertical movement of airflows with strong updraft and strong downdraft. In thunderstorms, both updrafts and downdrafts can occur in adjacent places. This contrast of positive and negative shear stress modulus is also clearly observed in Fig. 11d along three shear lines of airflows. The positive and negative shear stress modulus in Fig. 13d is determined by the convergence angles between different airflows and reflects the spatial distribution of ascending and descending airflows. The spatiotemporal variation of the shear stress modulus will form the spatiotemporal variation of dust concentration. It shows that the spatial and temporal distributions of shear stress have clear dynamic and physical significance.

From 20:10 BJT on 14 April to 08:10 BJT on 15 April 2021, the location of dust storm moved to the southeast with a strengthening trend. The distribution in Fig. 14 shows the spatial distribution of vorticity, divergence, total kinetic energy, and shear stress modulus at 08:00 BJT on 15 April 2021. On the vorticity and divergence plots (Fig. 14a and b), there is the greatest positive and negative values near the center of cyclone. From the spatial distribution, vorticity and divergence are not sufficient to indicate the specific extent of the dust storm. At this moment, the large value areas of total kinetic energy and shear stress modulus basically correspond to the domain of the dust storm so that the signal indicated the dust storm is obvious. However, there are no positive and negative bands in the total kinetic energy distribution (Fig. 14c). Positive and negative bands in the distribution of shear stress modulus can indicate the concentration fluctuation of airborne dust (Figs. 14d and 12b). One phenomenon showed that the large area of dust concentration in Fig. 12b has moved to China. However, why do the sand starting dynamic conditions indicated by the total kinetic energy and shear stress modulus occur in Mongolia? The reason is that the high dust concentration in northern China is drift from the source area over Mongolia.

7. Conclusions and discussion

The theoretical analysis shows that the orthogonal convergence of airflows can produce a significant non-zero shear stress modulus or high energy density. The shear stress modulus depends upon the angle of two adjacent air parcels for the cross convergence, while other two types (tailgating and head-on convergences) cannot. The maximum shear

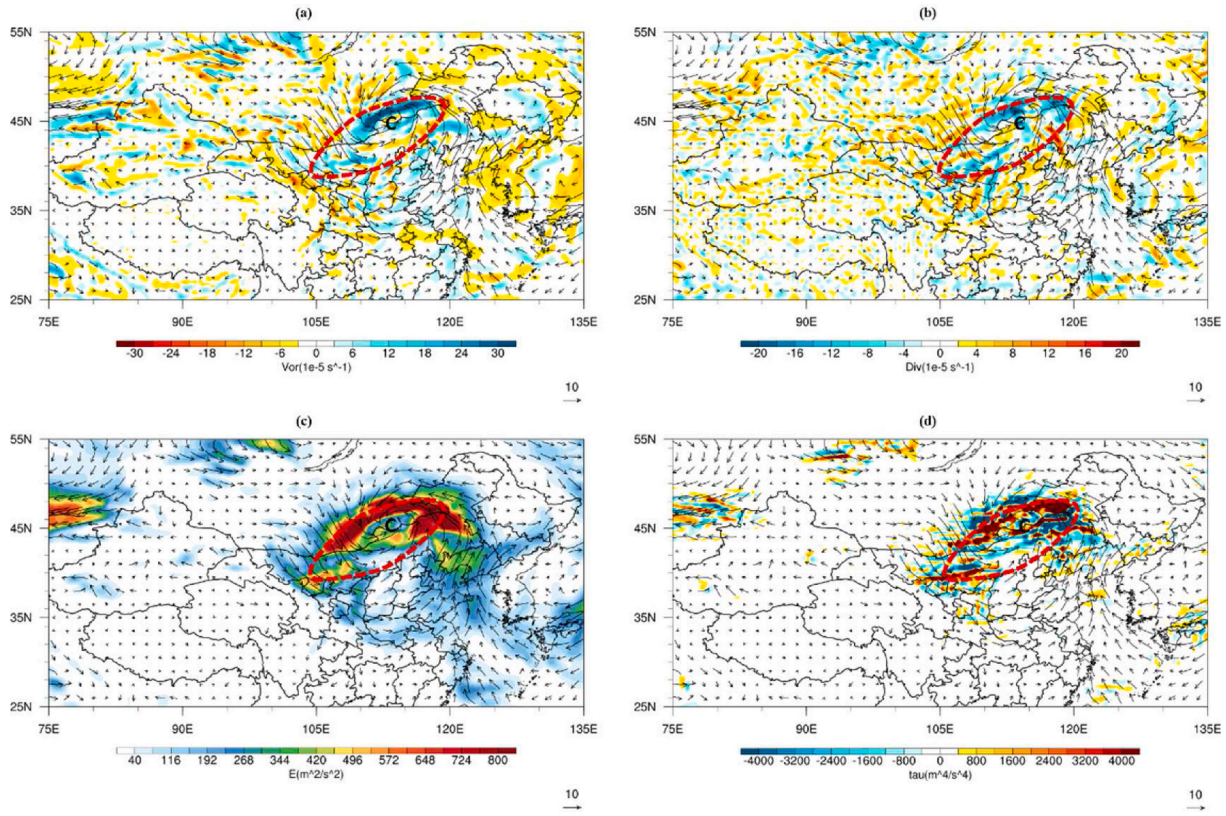

Fig. 14. Same as in Fig. 13 except at 08:00 BJT on 15 April 2021.

stress modulus can be found from the orthogonal convergence of four adjacent air parcels such as strong tropical cyclones (strong hurricanes and strong typhoons) with their Category 4 or 5. In most cases, the maximum shear stress modulus can form from two adjacent air parcels with orthogonal interaction.

The shear stress has two new vertical vectors produced by two adjacent parcels at their horizontal convergence point. Two important features are the direction and modulus of shear stress. Its modulus indicates new physical states of matter pointing the intensity of extreme weather. Its two directions are perpendicular to the plane constructed by two adjacent horizontal airflows. The shear stress can induce cyclonical and anti-cyclonical rotating vortices effected by the Coriolis force and new airflows, which enhance and maintain strong rising and sinking motions resulting in severe weather. This can explain why extreme weather and anomalous climate are often associated with the orthogonal convergence of two airflows. Therefore, the orthogonal convergence is a device for generating new energy density and altering motion directions of horizontal air parcels.

Tornadoes and hurricanes happened in the atmosphere are disastrous vortex systems. Their internal dynamics, especially for the formation of inner downdraft core and outer updraft ring, remain an unsolved mystery. In this study, the orthogonal interaction of horizontal anomalous airflows is used to understand the internal dynamics for generating tornadoes and hurricanes. A tornado with descending inner funnel-shaped vortex and ascending outer wall cloud is formed by the orthogonal convergence of lower tropospheric anomalous airflows. The near-ground updraft ring (outer wall cloud) surrounded the inner funnel-shaped vortex is the result of a recoil or collision when the downdraft airflows reach the ground. Sinking inner clear-sky eye and rising outer cloud shield of a strong hurricane are generated by the orthogonal convergence of upper tropospheric anomalous airflows at around 300 hPa and the horizontal convergence of anomalous airflow in the lower troposphere, respectively.

Around the center of tropical cyclones, extratropical cyclones, and meso-scale cyclones, low-level airflows converge in a cyclonic pattern. On the cyclonic shear line of anomalous airflows, their orthogonal convergence produces shear stresses, creating strong updraft and downdraft. This rotating downdraft forms a funnel-shaped vortex at the bottom of a cumulonimbus cloud, which is a tornado when it reaches the ground. Therefore, on the anomalous weather map of the lower atmosphere, the position of the orthogonal convergence of anomalous winds can be used for positioning tornadoes.

The appearance of inner clear-sky eye and outer cloud shield is a sign of the formation of a strong hurricane. The initial disturbances of most hurricanes are somewhat due to orthogonal interactions of anomalous trade winds in the lower troposphere. As the orthogonal convergence of large-scale anomalous airflows continues to strengthen, the condensation latent heat released over the convergence center forms a warm core and decreases the surface pressure, which has been described by the CISK theory. As a hurricane matures, the largest upper horizontal winds at around 300 hPa orthogonally converge so that the maximum shear stress forms the downdraft at the center of a hurricane. The formation of outer cloud shield can also be seen as a counteraction of the central eye downdraft. Finally, an inner clear-sky eye and outer cloud shield surrounding with the convergence of four spiral anomalous airflows form a typical structure of strong hurricane. Dynamically, a strong hurricane is equivalent to an amplified huge-size tornado.

People have long been looking for an extreme weather indicator that is both intuitive and simple, as well as has physically dynamic meaning. We give the shear stress modulus as an indicator of predicting extreme weather. The calculation results from tropical and extratropical cyclones showed that the shear stress modulus of anomalous airflows can indicate the domain of extreme weather events with wave-like fluctuations of internal cloud-rain distribution and airborne dust concentration, which has clear physical kinetic significance. The spatial distribution of the shear stress modulus and total kinetic energy of anomalous airflows can

indicate the domain of rainfall and dust storms, and their ability is superior to the anomalous wind vorticity, anomalous wind divergence and anomalous water vapor spatial distribution.

The two basic physical quantities in conventional weather diagnosis are vorticity and divergence. A near-surface cyclone is a low-pressure system that converges water vapor and heat near the ground toward the center. The positive vorticity corresponding to the low-pressure system indicates the intensity of air rotation, and the negative divergence indicates the intensity of air convergence to the center, but neither of them indicates the whereabout of air parcels for future. A new physical quantity given in this paper is shear stress. The shear stress calculated by the air parcels at the atmosphere not only has a modulus, but also has two directions. The shear stress modulus represents the new energy generated by the convergence interaction of air parcels. The direction of shear stress indicates where the new matter with new energy is going.

Extreme weather events are the result of atmospheric movements deviating from the normal climatic state and the release of anomalous energy. The three-dimensional structure linked with different extreme weather events can be visually observed from the anomalous variables which are obtained by the observational and model variables subtracting the climatic state. In the lower atmosphere, anomalous airflow convergence lines can indicate where extreme weather is occurring. Based on anomalous variables, the calculation of shear stress has its physically meaningful. The shear stress modulus indicates the intensity, location, and duration of extreme weather physically. Particularly, the direction of shear stress can indicate where the anomalous variable is going and what types of extreme weather will occur. Thus, shear stress should be used in daily weather forecasting. Numerical weather prediction models have been achieved a significant development during the last decades. To accurately and quantitatively predict extreme weather events, the shear stress modulus using anomalous winds needs to be addressed in both regional and global numerical weather prediction models.

Data statement

The fifth generation ECMWF atmospheric reanalysis (ERA5) data can be obtained from https://cds.climate.copernicus.eu/cdsapp#!/dataset/reanalysis-era5-pressure-levels. The airborne dust matter is from the Himawari-8 geostationary meteorological satellite of Japan Meteorological Agency (https://www.eorc.jaxa.jp/ptree).

CRediT authorship contribution statement

Weihong Qian: Conceptualization, Methodology, Writing – original draft, Writing – review & editing. **Jun Du:** Formal analysis, Writing – original draft, Writing – review & editing. **Jeremy Cheuk-Hin Leung:** Visualization. **Weijing Li:** Formal analysis. **Fangfang Wu:** Data curation. **Banglin Zhang:** Formal analysis, Funding acquisition.

Declaration of competing interest

All authors declare that there is no conflict of interest for this article.

Data availability

Data will be made available on request.

Acknowledgments

The author wishes to thank the two anonymous reviewers for constructive suggestions and comments that have improved the paper. This article commemorates Mr. Wang Shizhong, who graduated from Physical Department of Southwest Associated University in China and was former chief engineer of Jiangsu Meteorological Bureau. The concept of shear stress described in this paper is similar to the "updrag force" task that he assigned to the first author to investigate thirty-nine years ago. The work was supported by the innovative R&D project in Guangdong Province in China (2019ZT08G669) and the National Natural Science Foundation of China (41775067).

References

Bassill, N.P., 2014. Accuracy of early GFS and ECMWF Sandy (2012) track forecasts: evidence for a dependence on cumulus parameterization. Geophys. Res. Lett. 41, 3274–3281.
Barry, R.G., Chorley, R.J., 1992. Atmosphere, Weather, and Climate, sixth ed. Routledge, London. 979-0-415-07760-6.
Beall, J., 2012. Extreme weather: a guide to surviving flash floods, tornadoes, hurricanes, heat waves, snowstorms, tsunamis and other natural disasters. Libr. J. 137 (1), 129-129.
Burger, J., Gochfeld, M., 2014. Perceptions of personal and governmental actions to improve responses to disasters such as Superstorm Sandy. Environ. Hazards 13, 200–210.
Brunet, G., Parsons, D.B., Ivanov, D., et al., 2023. Advancing weather and climate forecasting for our changing world. Bull. Am. Meteorol. Soc. 104 (4), E909–E927.
Cai, W.J., Lengaigne, M., Borlace, S., et al., 2012. More extreme swings of the South Pacific convergence zone due to greenhouse warming. Nature 488 (7411), 365–369.
Ding, Y.H., Chan, J.C.L., 2005. The East Asian summer monsoon: an overview. Meteorol. Atmos. Phys. 89, 117–142.
Dowdy, A.J., Catto, J.L., 2017. Extreme weather caused by concurrent cyclone, front and thunderstorm occurrences. Sci. Rep. 7, 40359.
Gibney, E., 2022. How the revamped large hadron collider will hunt for new physics. Nature 605, 604–607.
Han, W.Q., Meehl, G.A., Hu, A.X., et al., 2017. Decadal variability of the Indian and Pacific Walker cells since the 1960s: do they covary on decadal time scales? J. Clim. 30 (21), 8447–8468.
Hu, Y.M., et al., 2013. Precipitation patterns during the "Dragon boat water" in South China for the recent 49 years. Meteorol. Mon. 39, 1031–1041 (in Chinese).
Knupp, R.K., Murphy, T.A., Coleman, T.A., et al., 2014. Meteorological overview of the devastating 27 April 2011 tornado outbreak. Bull. Am. Meteorol. Soc. 95 (7), 1041–1062.
Lavers, D.A., Ramos, M.H., Magnusson, L., et al., 2020. A vision for hydrological prediction. Atmosphere 11 (3), 237.
Lee, J.J., Kim, C.H., 2012. Roles of surface wind, NDVI and snow cover the recent changes in Asian dust storm occurrence frequency. Atmos. Environ. 59, 366–375.
Li, Y., Wu, Z.Y., He, H., Lu, G.H., 2021. Deterministic and probabilistic evaluation of subseasonal precipitation forecasts at various spatiotemporal scales over China during the boreal summer monsoon. Atmosphere 12 (8), 1049.
Lindstrom, C.A., D'Arcy, R., Garland, M.J., Gonzalez, P., et al., 2020. Matching small beta functions using centroid jitter and two beam position monitors. Phys. Rev. Accel. Beams 23, 052802.
Liu, R.Z., 2021. Latest trends of atmospheric cells under global warming. In: 3rd International Forum on Geoscience and Geodesy (IFGG). Book Series, 012003, 658.
Liu, J.J., Ding, Y.H., He, J.H., 2003. The structure analysis of a typical Meiyu front. Acta Meterol. Sinica 61 (3), 291–301.
Mathur, M.B., 1998. Development of an eye-wall like structure in a tropical cyclone model simulation. Dynam. Atmos. Oceans 27 (1–4), 527–547.
Martínez, M.A., Ruiz, J., Cuevas, E., 2009. Use of SEVIRI images and derived products in a WMO sand and dust storm warning system. IOP Conf. Ser. Earth Environ. Sci. 7, 012004.
Molinari, J., Vollaro, D., 2000. Planetary- and synoptic-scale influence on eastern Pacific tropical cyclogenesis. Mon. Weather Rev. 128 (9), 3296–3307.
Moron, V., Robertson, A.W., Pai, D.S., 2017. On the spatial coherence of sub-seasonal to seasonal Indian rainfall anomalies. Clim. Dynam. 49 (9–10), 3403–3423.
Moraes, J.S., Pakter, R., Rizzato, F.B., 2005. Centroid motion in periodically focused beams. Phys. Plasmas 12, 023104, 2005.
Normile, D., Cho, A., 2019. Physicists brace for decision on Japan's international linear collider. Science 363, 911–912.
Pan, G.S., Hu, Q.R., Gu, W., et al., 2021. Assessment of plum rain's impact on power system emissions in Yangzte-Huaihe River basin of China. Nat. Commun. 12 (1), 6156.
Qian, W.H., 2017. Temporal Climatology and Anomalous Weather Analysis. Springer Atmospheric Sciences.
Qian, W.H., 2022. Orthogonal collision of particles produces new physical state. J. Mod. Phys. 13, 1440–1451.
Qian, W.H., Huang, J., Zhang, G.W., 2016a. Reexamining the binary interaction of four pairs of tropical cyclones in the Northwest Pacific. J. Meteorol. Soc. Jpn. 94, 303–322.
Qian, W.H., Huang, J., Du, J., 2016b. Examination of Hurricane Sandy's (2012) structure and intensity evolution from full-field and anomaly-field analyses. Tellus-A 68, 29029.
Qian, W.H., Leung, J.C.H., Jin, R.H., Fu, J.L., Wu, F.F., Kuang, Z.J., Du, J., 2017. Application of anomalous variables to severe convective system analyses and model evolution: a case study on tornado-producing anomalous systems near Lixia River, Jiangsu Province. Meteorol. Mon. 43 (2), 166–180 (in Chinese).
Qian, W.H., Leung, J.C.H., Luo, W.M., Du, J., Gao, J.D., 2019. An index of anomalous convective instability to detect tornadic and hail storms. Meteorol. Atmos. Phys. 131 (3), 351–373.

Qian, W.H., Du, J., Ai, Y., 2021a. A review: anomaly-based versus full-field-based weather analysis and forecasting. Bull. Am. Meteorol. Soc. 102 (4), E849–E870.
Qian, W.H., Ai, Y., Chen, X.C., 2021b. Anomalous synoptic environments of a strong convective process with tornado in Kaiyuan City, Liaoning Province. Chin. J. Geophys. 64 (5), 1531–1541 (in Chinese).
Qian, W.H., Leung, J.C.-H., Ren, J., Du, J., Feng, Y., Zhang, B., 2022. Anomaly based synoptic analysis and model prediction of six dust storms moving from Mongolia to northern China in Spring 2021. J. Geophys. Res., [Atmos.] 127, e2021JD036272.
Qian, W., Leung, J., Zhang, B., 2023. An orthogonal collision dynamic mechanism of wave-like uplift plateaus in southern Asia. Open J. Geol. 13, 828–846.
Qin, D.Y., Fang, Z.Y., Jiang, J.X., 2006. The cloud systems of heavy rainfall in the typical Meiyu period and their interactions. Chin. J. Atmos. Sci. 30 (4), 578–586 (in Chinese).
Rasmussen, E.N., Straka, J.M., 2007. Evolution of low-level angular momentum in the 2 June 1995 Dimmitt, Texas, tornado cyclone. J. Atms. Sci. 64, 1365–1378.
Seo, K.H., 2021. Vertical vorticity structure associated with the boreal summer intraseasonal oscillation: Barotropic or Baroclinic? Atmosphere 22 (2), 259–265.
Sun, J.H., Fu, S.M., Fu, S.M., et al., 2023. Primary characteristics of the extreme heavy rainfall event over Henan in July 2021. Atmos. Sci. Lett. 24 (1).
Wang, L.J., He, J.H., Guan, Z.Y., 2006. Climatological features of East Asian subtropical summer monsoon trough and its comparison with South China Sea summer monsoon trough. Acta Meterol. Sinica 64 (5), 583–593.
Yamamoto, K., 2016. Dust Detection Using IR Channels of Himawari-8 Univ. Wisconsin-madison, pp. 1–63.
Yoshino, M.M., 1968. Intertropical convergence zone and polar frontal zone over northwest Pacific and its surrounding areas and their relation to some climatological significances. Bull. Am. Meteorol. Soc. 49 (2), 141.
Yuan, T., Qie, X.S., 2008. Study on lightning activity and precipitation characteristics before and after the onset of the South China Sea summer monsoon. J. Geophys. Res., [Atmos.] 113 (D14).
Zhao, D.J., Chen, L.S., Yu, Y.B., 2021. Monsoon surges enhance extreme rainfall by maintaining the circulation of landfalling tropical cyclones and slowing down their movement. Front. Earth Sci. 9 https://doi.org/10.3389/feart.2021.717447.